www.acsnano.org

# Bidi Mag Rato ChangH

# Bidirectional Droplet Manipulation on Magnetically Actuated Superhydrophobic Ratchet Surfaces

ChangHee Son, Zhengyu Yang, Seungbeom Kim, Placid M. Ferreira, Jie Feng, and Seok Kim\*





**ACCESS** I

Downloaded via UNIV ILLINOIS URBANA-CHAMPAIGN on September 24, 2024 at 15:14:48 (UTC). See https://pubs.acs.org/sharingguidelines for options on how to legitimately share published articles.

III Metrics & More

Article Recommendations

Supporting Information

ABSTRACT: Droplet manipulation has garnered significant attention in various fields due to its wide range of applications. Among many different methods, magnetic actuation has emerged as a promising approach for remote and instantaneous droplet manipulation. In this study, we present the bidirectional droplet manipulation on a magnetically actuated superhydrophobic ratchet surface. The surface consists of silicon strips anchored on elastomer ridges with superhydrophobic black silicon structures on the top side and magnetic layers on the bottom side. The

Bi-directional Droplet Manipulation

Superhydrophobic Ratchet Surfaces

Droplet

External Magnet

soft magnetic properties of the strips enable their bidirectional tilting to form a ratchet surface and thus bidirectional droplet manipulation upon varying external magnetic field location and strength. Computational multiphysics models were developed to predict the tilting of the strips, demonstrating the concept of bidirectional tilting along with a tilting angle hysteresis theory. Experimental results confirmed the soft magnetic hysteresis and consequential bidirectional tilting of the strips. The superhydrophobic ratchet surface formed by the tilting strips induced the bidirectional self-propulsion of dispensed droplets through the Laplace pressure gradient, and the horizontal acceleration of the droplets was found to be positively correlated with the tilting angle of the strips. Additionally, a finite element analysis was conducted to identify the critical conditions for dispensed droplet penetration through the gaps between the strips, which hinder the droplet's self-propulsion. The models and findings here provide substantial insights into the design and optimization of magnetically actuated superhydrophobic ratchet surfaces to manipulate droplets in the context of digital microfluidic applications.

KEYWORDS: droplet manipulation, magnetic actuation, superhydrophobic ratchet surface, transfer printing, Laplace pressure gradient, digital microfluidics, soft magnetic properties

roplet manipulation has gained significant research interest due to its applicability in surface cleaning, <sup>1,2</sup> water harvesting, <sup>3</sup> chemical reactions, <sup>4,5</sup> cell culture, <sup>6</sup> material synthesis, <sup>7</sup> bioassay, <sup>8</sup> and biosensors. <sup>9</sup> Various methods have been devised for droplet manipulation, including electric and magnetic field, thermal, acoustic, light-based ones, and passive manipulation through surface structure modifications. <sup>10,11</sup> Among those, magnetic actuation has emerged as a promising approach due to its advantages of remote and instantaneous droplet control. <sup>12</sup> Particularly, magnetic digital microfluidics offers scalability for handling larger volumes and higher tolerance to variations in liquid properties. <sup>13</sup>

Several methods exist for manipulating droplets by using a magnetic field. One common approach involves using magnetic particles or beads to drive the droplets.<sup>8,14–21</sup> The droplet is placed on a substrate, which may be hydrophobic, and magnetic particles or beads are immersed in the droplet, enabling its manipulation by application of an external magnetic field. Depending on the speed of the magnetic particles or beads, the droplet can either follow them, utilizing surface tension, or they

can be separated. Additionally, droplets themselves can exhibit an attraction to external magnetic fields. Ferrofluidic droplets, which are mixtures of magnetic particles and oil, <sup>22–26</sup> or magnetic liquid marbles, where a droplet is covered with magnetic particles, <sup>27–31</sup> can be utilized for droplet manipulation.

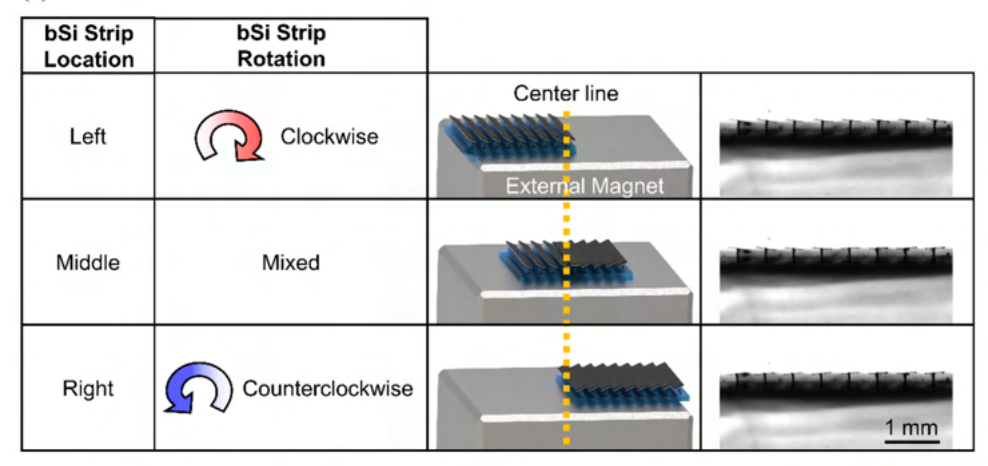
Another method of droplet manipulation involves adjusting the surface structure of the substrate. Localized shrinking of the substrate can create a temporary basin area, causing a droplet to move toward it, and the location of the basin, acting as the droplet's destination, can be modified using an external magnetic field.  $^{32,33}$  Alternatively, micropillars or grooves with dimensions below 50  $\mu$ m can appear or disappear upon the

Received: August 7, 2023 Accepted: October 13, 2023 Published: October 19, 2023





(a)



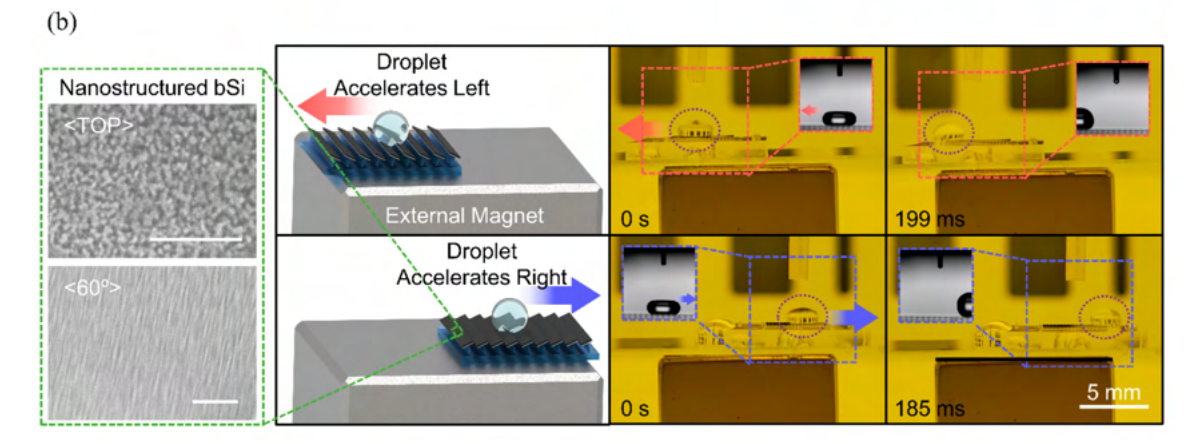


Figure 1. Demonstrations of bidirectional droplet manipulation capabilities. (a) The bSi strips rotating in different directions depending on their location relative to an external magnet. (b) The water droplet being manipulated in different directions based on the switchable tilting direction of the bSi strips. The green-outlined magnified image in the first column indicates the nanostructured bSi captured from the scanning electron microscope. The scale bar represents  $1\mu m$ , and both the top view and  $60^{\circ}$  diagonal view are shown. The red and blue inset images in the following rows represent the images captured from a high-speed camera.

application of an external magnetic field to either halt or initiate droplet manipulation. 34–37 Research has also been conducted on larger pillars, where ferromagnetic particles are incorporated into elastomer pillars 38–46 or shape memory polymers. 47 Moreover, designs for magnetic field actuated droplet manipulation devices have been proposed. Wang et al. 48 proposed a shutter shaped surface where microblades are connected to a fixed frame using elastomer cords. The microblades act as shutters, allowing droplet manipulation upon the application of external magnetic fields. Yang et al. 49 have developed a superhydrophobic electromagnet needle capable of picking up, transporting, splitting and placing the magnetic droplets. Zhou et al. 50 presented a 3D printed magnetic robot actuator that can be controlled for gripping or pushing a droplet.

More recently, our previous study showed the assembly of superhydrophobic silicon platelets onto the ferromagnetic-elastomer pillars using transfer printing, creating a hierarchical structure to manipulate droplets. We further advanced this structure by sputtering a layer of neodymium—iron—boron (NdFeB) onto the backside of the superhydrophobic silicon platelets eliminating the need for incorporating ferromagnetic particles inside the pillars. Both studies adopted the Laplace pressure gradient of a droplet generated on the super-

hydrophobic ratchet surface to manipulate it but with limited droplet motion analysis based on a simple hard-magnet model.

Additionally, the utilization of magnetic forces as an external stimulus for droplet manipulation offers the distinct advantage of controlling the direction of the droplet acceleration. To the best of our knowledge, magnetically actuated bidirectional droplet manipulation has not been previously demonstrated but Feng et al. <sup>53</sup> showcased a bidirectional liquid manipulation on a 3D printed Araucaria leaf-inspired surface which does not require the external stimuli. This surface achieved selective liquid spreading based on the liquid's surface tension, presenting promising prospects for various practical applications. However, the magnetic stimulus method presented in our work excels in enabling the bidirectional manipulation of the droplets even with the same properties, thus offering a different approach to this capability.

This work shows a more in-depth investigation of the superhydrophobic ratchet surface based on a complete soft-magnet model in terms of its bidirectional droplet manipulation abilities. The surface includes silicon strips anchored to elastomer ridges by transfer printing. This heterogeneous integration capitalizes on the advantageous properties, of silicon, such as having nanostructures and excellent thermal properties, while preserving the flexible manipulation capabilities of the

elastomer ridges. The top side of the strips has superhydrophobic black silicon (bSi) structures with a single layer of perfluorodecyltrichlorosilane (FDTS) and the bottom side of the strip has magnetic layers. Therefore, these bSi strips tilt upon an external magnetic field, creating a superhydrophobic ratchet surface. When a droplet is dispensed on the surface, it is selfpropelled by the Laplace pressure gradient, which is determined by the tilting angle of the bSi strips. Furthermore, we present a bidirectional droplet manipulation method that capitalizes on the soft magnet properties of nanoparticle magnetic layers. While NdFeB is commonly known as a hard magnet with high coercivity, we exploit the phenomenon where the coercivity decreases significantly when the grain size is below 50 nm. 54-56 Leveraging this phenomenon, our bSi strips with sputtered nanoparticle NdFeB can repetitively undergo demagnetization and remagnetization in the opposite pole direction by making slight adjustments to the external magnetic field. Figure 1a illustrates this behavior, with the bSi strips rotating clockwise when placed on the left side of the external magnet and counterclockwise when placed on the right side of it. This characteristic enables bidirectional droplet manipulation on our ratchet surface by selectively adjusting the external magnetic field, as demonstrated in Figure 1b, Movie S1 and Movie S2. The subsequent sections include an analysis of the soft magnetic physics using MATLAB simulations, providing evidence of the observed tilting angle hysteresis behavior. Additionally, we present the analytical and experimental tilting angles of the ratchet surface and investigate their influence on droplet selfpropulsion acceleration. Next, we experimentally tested the effect of the potential energy of a dispensed droplet on its selfpropulsion. Lastly, we developed a finite element analysis (FEA) model to pinpoint the conditions that allow seamless manipulation of the droplet.

# **RESULTS AND DISCUSSION**

Computational Multiphysics Modeling of Magnetoresponsive bSi Strips. The magnetoresponsive bSi strips we propose possess the capability to enable bidirectional droplet manipulation, an attribute owed to their soft magnetic behavior. While NdFeB is generally considered a hard magnetic material, the coercivity of magnetic materials can diminish at a rate proportional to the sixth power of its dimensions when its grain size falls below 50 nm. 54 We were able to take advantage of this behavior to acquire a soft magnetic NdFeB layer by reducing the sputtering rate to 6.7 nm/min. As a result, we were able to obtain bSi strips with extremely low coercivity capable of repetitive demagnetization and remagnetization in the opposite pole direction through the variation of the external magnetic field along the strips' width direction. This behavior of the bSi strip, constantly switching its pole direction, is also demonstrated in Figure S1 and Movie S3. In this section, we introduce the mathematical equations that govern the external magnetic field of a permanent magnet. We also establish an equilibrium equation accounting for both the magnetic torque and the elastic restoration torque governing the tilting of the bSi strips. Utilizing these equations, we computationally determined the tilting angle of the bSi strips based on their location and the strength of the external magnetic field.

To solve our computational model, we first derived a mathematical expression for the external magnetic fields. The magnetic field strength, represented as  $\overrightarrow{H_{\text{tot}}}(x, y, z) = \overrightarrow{H_x}(x, y, z) + \overrightarrow{H_z}(x, y, z)$ , for a cuboid

permanent magnet with width, length, and height of 2a, 2b, and 2c, respectively, and with the origin of the Cartesian coordinate system at its center of mass, as illustrated in Figure 2a. We assume that the *y*-component of the magnetic field

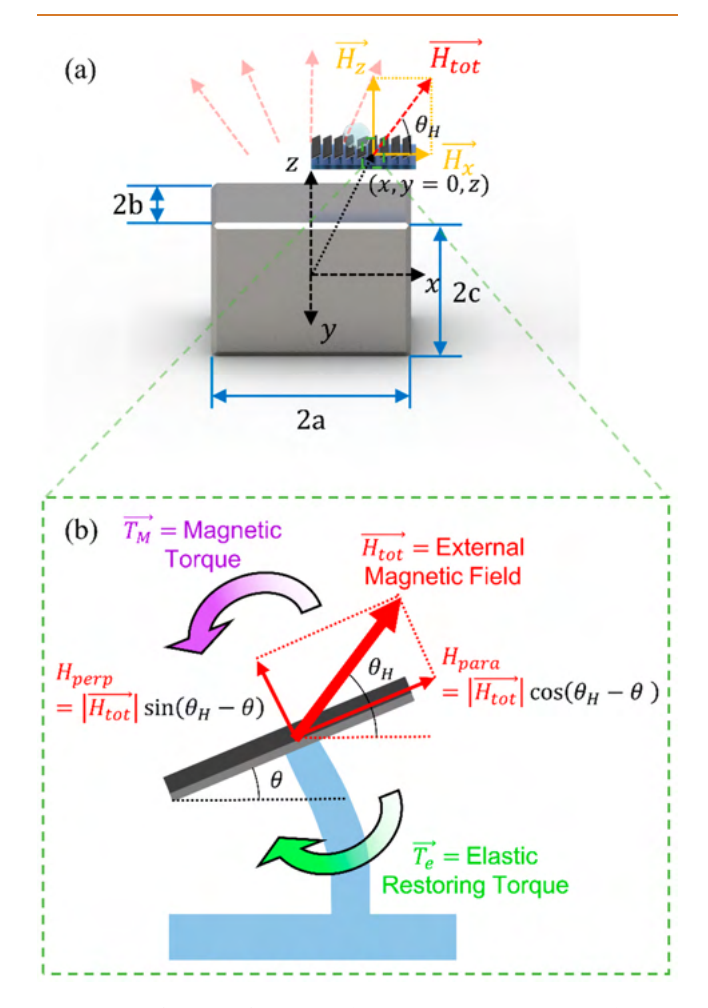


Figure 2. Definition of the Coordinate System, Magnetic Field, and torque equilibrium. The illustration depicting (a) the external magnetic field generated by a cuboid permanent magnet and (b) the equilibrium of torques applied to the bSi strip.

strength can be disregarded because the center of the bSi strips is placed at y = 0. The components that make up the total magnetic field strength can be calculated using the following equations:<sup>57</sup>

$$H_{x}(x, y, z) = \frac{M_{e}}{4\pi} \ln \frac{F_{2}(-x, y, -z)F_{2}(x, y, z)}{F_{2}(x, y, -z)F_{2}(-x, y, z)}$$
(1)

$$H_{z}(x, y, z) = \frac{M_{e}}{4\pi} [F_{1}(-x, y, z) + F_{1}(-x, y, -z) + F_{1}(-x, -y, -z) + F_{1}(-x, -y, -z) + F_{1}(x, y, z) + F_{1}(x, y, -z) + F_{1}(x, -y, z) + F_{1}(x, -y, -z)]$$

$$(2)$$

Here,  $M_e$  is the magnetization of the external magnet and the functions  $F_1$  and  $F_2$  above are defined as

$$F_{1}(x, y, z) = \tan^{-1} \frac{(x+a)(y+b)}{(z+c)\sqrt{(x+a)^{2}+(y+b)^{2}+(z+c)^{2}}}$$
(3)

$$\frac{\sqrt{(x+a)^2 + (y-b)^2 + (z+c)^2} + b - y}{\sqrt{(x+a)^2 + (y+b)^2 + (z+c)^2} - b - y}$$
(4)

Evidently, the magnitude of the total magnetic field  $|H_{\text{tot}}|$  can be calculated as  $\sqrt{{H_x}^2 + {H_z}^2}$  and its angle  $\theta_H$  as  $\tan^{-1}\frac{H_z}{H_u}$ .

Thus far, our discussion has primarily focused on the cuboid magnet. However, should a cylindrical magnet be employed, the mathematical expressions for its external magnetic fields can be found in Figure S2 and the Supporting Information. 58,59

To derive an analytical solution for the tilting angle  $\theta$  of the bSi strip, we utilize an equilibrium equation that accommodates two opposing torques acting on the bSi strip. One of these torques is the elastic restoring torque  $\overrightarrow{T_e}$ , the magnitude of which can be expressed as

$$|\overrightarrow{T_e}| = c_0 \frac{EI}{L} \theta \tag{5}$$

In this equation,  $c_0$  represents a parametric angle coefficient, while E, I, and L denote the Young's modulus, the second moment of inertia, and the height of the elastomer ridge, respectively.

The counteracting torque in the equilibrium equation is the magnetic torque  $\overrightarrow{T_M}$  which can be formulated as follows

$$\overrightarrow{T_M} = \overrightarrow{V_m M} \times \overrightarrow{H_{\text{tot}}} = \overrightarrow{V_m M} \times \overrightarrow{H_{\text{perp}}}$$
(6)

In this equation,  $\vec{M}$  and  $V_m$  refer to the magnetization and volume of the sputtered NdFeB, respectively. Furthermore,

 $H_{\mathrm{perp}}$  represents the component of the external magnetic field that is perpendicular to the bSi strip, and its magnitude can be calculated as  $|\overrightarrow{H}_{\mathrm{tot}}|\sin(\theta_H-\theta)$ . As a result, we can substitute eqs 5 and 6 into the equilibrium equation  $|\overrightarrow{T_e}|=|\overrightarrow{T_m}|$  yielding

$$c_0 \frac{EI}{L} \theta = V_m |\overrightarrow{M}| |\overrightarrow{H}_{tot}| \sin(\theta_H - \theta)$$
(7)

In this equation, all variables are known except for the magnetization  $\vec{M}$  of the sputtered NdFeB on the bSi strips. This can be determined through the magnetic hysteresis graph depicted in Figure S3. The *y*-value of the graphs is in Figure S3 represents magnetization of NdFeB which is the function of the strength of the external magnetic field applied in parallel to the bSi strips, denoted as  $H_{\text{para}}$ , as illustrated in Figure 2b. The value of  $H_{\text{para}}$  continuously changes depending on the location and resulting tilting angle of the bSi strips, causing the magnetization of the bSi strips to constantly shift along the magnetic hysteresis loop.

The bSi strip first gets initially magnetized from point o to point a, as shown in Figure S3a. If the external magnetic field strength,  $H_{\text{para}}$ , is substantial enough to reach the red region in Figure S3b, then the magnet is considered to be positively saturated. Conversely, if  $H_{\text{para}}$  switches direction into the blue region, the magnet is considered to be negatively saturated.

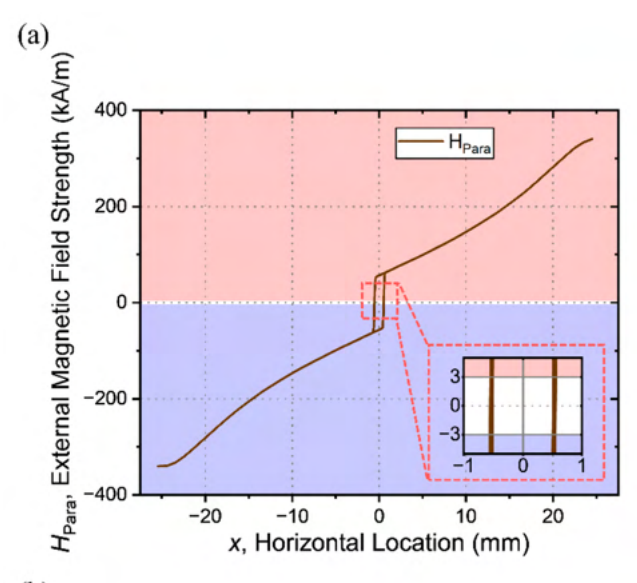
When  $H_{\rm para}$  is removed following initial magnetization, the graph traces the path from point a to b in Figure S3c, with point b referred to as remanence. If a negative  $H_{\rm para}$  is applied, the graph intersects with the x-axis at point c, known as the coercivity, beyond which the magnet no longer exhibits magnetization. As more negative  $H_{\rm para}$  is applied, the magnet follows the path from point c to d in Figure S3d, resulting in negative saturation. Next, if  $H_{\rm para}$  increases again, the graph traces a different path from point d to e to f and back to a, as shown in Figure S3e,f, thereby achieving positive saturation once more. In this context, points e and f represent remanence and coercivity in the opposite direction, respectively.

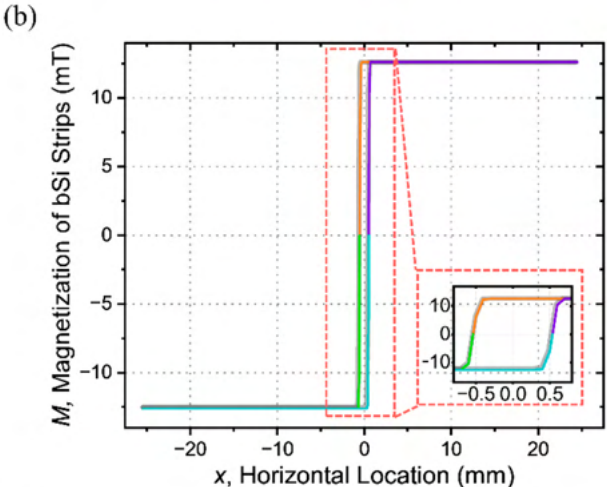
Eq 7 can now be numerically solved using MATLAB, with the results presented in Figure 3. The external permanent magnet chosen for our experiments was a cube with each edge measuring 50.4 mm. The distance between the bSi strips and the surface of the magnet was set at 5 mm. It is noteworthy to mention that not only does the magnetization  $\vec{M}$  display hysteresis behavior, but also  $H_{\text{para}}$  and  $\theta$ . Figure 3a presents the hysteresis loop for  $H_{\text{para}}$ , where the red region exceeds 3 kA/m, thereby positively saturating the bSi strips. Conversely, the blue colored region falls below -3 kA/m, leading to negative saturation of the bSi strips. The region where  $H_{\text{para}}$  does not saturate the bSi strips is magnified in the inset plot. Further plots representing other magnetic field strengths such as  $H_{\text{tot}}$   $H_{xy}$   $H_{yy}$  and  $H_{\text{perp}}$  are provided in Figure S4.

Figure 3b shows the magnetization M of bSi strips depending on their horizontal location with a hysteresis behavior. Here, we can observe that the  $\vec{M}$  is almost either positively or negatively saturated across the entire x-axis. A positive  $\vec{M}$  causes the bSi strips to rotate in a counterclockwise direction, which results in a positive value of the tilting angle  $\theta$  of the bSi strips, as depicted in Figure 3c. Conversely, a negative  $\vec{M}$  causes a corresponding clockwise rotation. The magnitude of  $\theta$  decreases as the distance from the center of the magnet x increases, which can primarily be attributed to the reduction in the perpendicular component of the magnetic field strength  $H_{\rm perp}$ .

The hysteresis behavior and bidirectional rotation of the bSi strips, as predicted from our computational multiphysics modeling, have been confirmed through the experiment depicted in Figure 4. At first, the red highlighted bSi strip seen in Figure 4a is located at x < -0.5 mm. Here, its magnetization Mis negatively saturated and the tilting angle  $\theta$  exhibits maximum negative rotation. As the bSi strip is translated toward the positive x direction, the  $\theta$  traces the lower part of the hysteresis loop, as illustrated in Figure 4b. If the red highlighted bSi strip continues to shift further, surpassing x > 0.5 mm as indicated in Figure 4c, its M becomes positively saturated and the  $\theta$  reaches the maximum positive rotation. In Figure 4d, when the bSi strip returns to the same position as in Figure 4b, the  $\theta$  of the redhovered bSi strip differs from its initial state. This is because the  $\theta$  trace the upper portion of the hysteresis loop as the bSi strip retracts. This phenomenon showcases both the inherent hysteresis behavior of the system and its capability for bidirectional operation.

**Droplet Propulsion on a Superhydrophobic Ratchet Surface.** A droplet dispensed on a superhydrophobic ratchet surface can exhibit self-propulsion due to the asymmetry of its shape. The major force that causes the actuation of the droplet is the Laplace pressure gradient, which can be expressed as 61-64





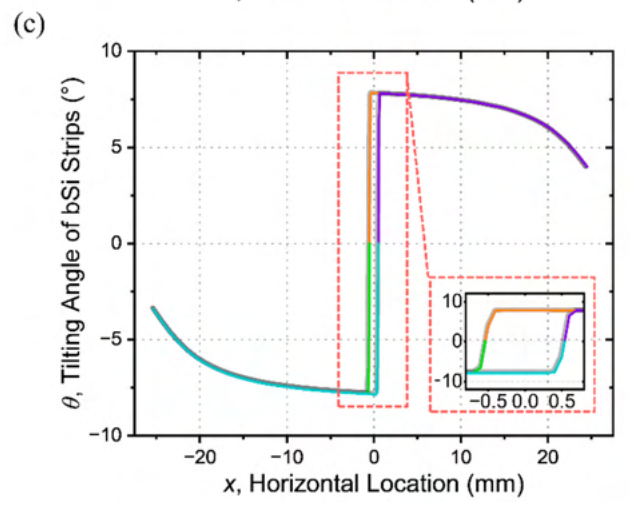


Figure 3. Results of computational modeling. (a) The magnitude of the external magnetic field strength parallel to the bSi strips, which contributes to their magnetization, depending on the horizontal location. (b) The magnitude of the magnetization depending on the bSi strip's location. (c) The resulting tilting angle of the bSi strips depending on the horizontal location. The inset plot magnifies the corresponding dashed box area for each panel.

$$F_L \approx 2\gamma \left(\frac{1}{R_t} - \frac{1}{R_l}\right) \times A_{yz}$$
 (8)

where  $\gamma$  represents the droplet's surface tension,  $R_l$  and  $R_t$  are the principal radii of curvature for the droplet's leading and trailing surfaces, respectively, and  $A_{yz}$  stands for the droplet's cross-sectional area perpendicular to the direction of motion. The tilting angle of the bSi strips  $\theta$  composing the ratchet surface induces a difference in contact angle between the leading and trailing sides of the droplet. Here, the leading side is the direction of the bSi strips' inclination, and the contact angle on this side is smaller by  $2\theta$  than the trailing side. This effect causes  $1/R_l$  to be smaller than  $1/R_b$  as shown in Figure SS, thereby accelerating the droplet toward the leading side. Moreover, an increase in  $\theta$  further augments the difference between the two contact angles, subsequently enhancing the force exerted on the droplet.

This relationship, where the tilting angle of the bSi strips  $\theta$ positively correlates with the horizontal propulsion force, was experimentally observed and is illustrated in Figure 5. First, we evaluated the distance between the bSi strips and the surface of the external magnet. Figure 5a represents the variation of  $\theta$ depending on the location of the bSi strip and the distance from the external magnet surface, calculated using the model we discussed in the previous section. Correspondingly, Figure 5b provides a snapshot of the actual tilt of the bSi strips depending on the distance from the magnet surface. As shown in Figure 5c, a droplet is dispensed onto the ratchet surfaces from a needle with a diameter of 500  $\mu m$  under five different conditions characterized by unique  $\theta$  values. While the droplet is dispensed and impacts the surface at the same location in all cases, the subsequent horizontal acceleration during the propulsion phase varies, depending on the value of  $\theta$ . The source of these captured images is Movie S4, which can be found in the Supporting Information. The movie was edited to synchronize the moment of impact across all five conditions.

The centroid position of the droplet in each frame of the movie was determined through image processing, as shown in Figure S6a. The horizontal position of the droplet's centroid is then plotted, with the results displayed in Figure S6b. Subsequently, the position data was differentiated using Savitzky-Golay Smoothing, using a window of 200 points and a second-order polynomial. The results, which show the horizontal velocity of the droplet, are plotted in Figure 5d as a solid line. The dashed lines on the same plot are the results from linear regression for the five different conditions, where the slope represents the average horizontal acceleration. These slopes are plotted in Figure 5e along with  $\theta$ , with both values presented as functions of the distance between the bSi strips and the surface of the external magnet. The result apparently has shown the positive correlation between  $\theta$  and the horizontal acceleration which was induced from the Laplace pressure gradient mentioned above.

To investigate the droplet propulsion on the ratchet surface further, we carried out an additional experiment, dispensing a droplet onto a superhydrophobic ratchet surface while varying the impact speed. This experiment is designed to confirm the effect of the potential energy on droplet propulsion when the tilting angle of the bSi strips is fixed. Figure 6a presents frames extracted from Movie S5 (available in the Supporting Information), showcasing the phases of the droplet of falling, impacting, and moving horizontally for different impact speeds. Using the same image processing technique mentioned in the

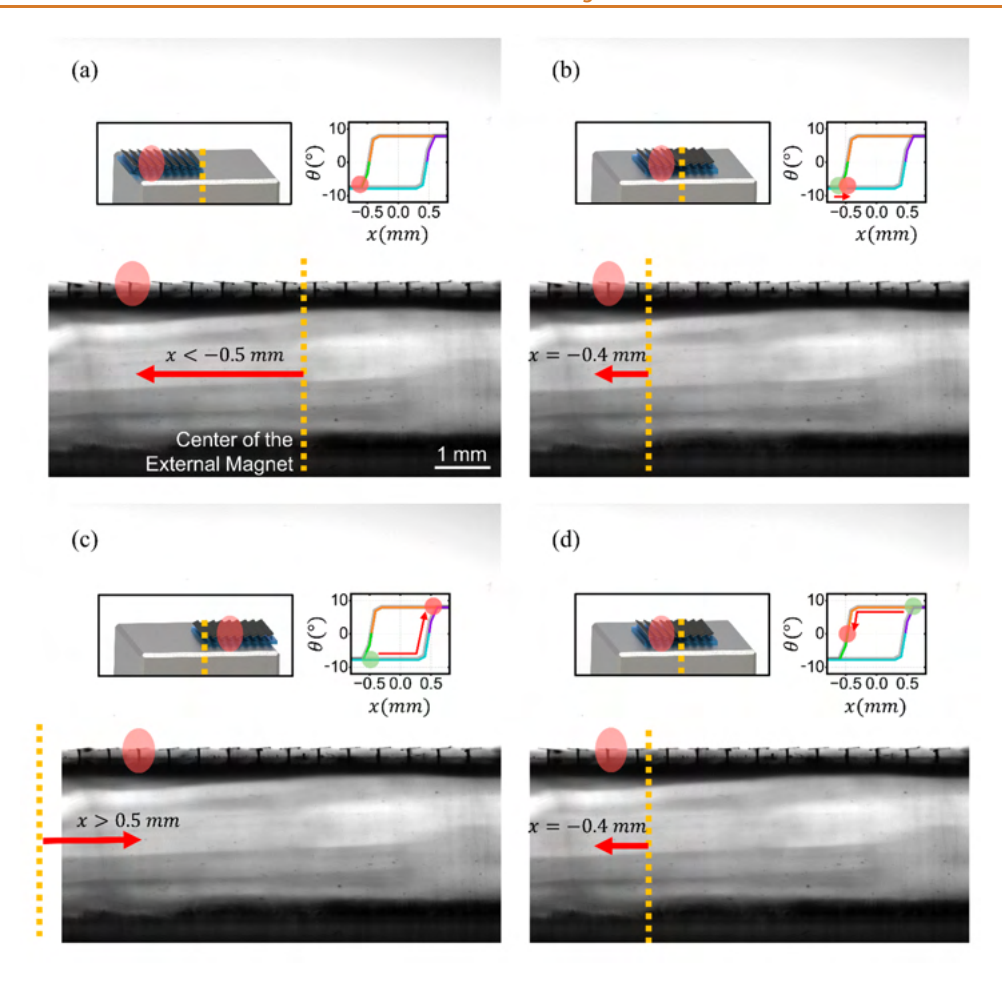


Figure 4. Experimental results showing the angle hysteresis behavior of the red highlighted bSi strip. (a) At x < -0.5 mm, the bSi strip is negatively saturated. (b) At x = -0.4 mm, the bSi strip still exhibits negative saturation. (c) However, when the bSi strip moves to x > 0.5 mm, it switches to positive saturation. (d) Upon returning to x = -0.4 mm, the bSi strip exhibits a different tilting angle compared to (b), even though it is located at the same position. The inset graphic provides an approximate location of the bSi strips on the external magnet, while the plot illustrates the calculated tilting angle based on the computational model.

previous section, we determined the position of the droplet's centroid in each frame of the movie. The corresponding horizontal and vertical positions are plotted in Figure S7a and S7b, respectively. Subsequently, both the horizontal and vertical position data were differentiated using Savitzky-Golay Smoothing, with a second-order polynomial and window sizes of 200 and 50 points, respectively. Here, the impact speed  $\nu$  right before the droplet touches the ratchet surface was obtained from the vertical velocity, as shown in Figure S7c. The corresponding horizontal velocity is illustrated as a solid line in Figure 6b. The dashed lines in the same plot are the results from polynomial fitting for the six different conditions, where the slope represents the average horizontal acceleration. The average horizontal acceleration for each impact speed is graphed in Figure S7d. These results indicate that there is not a direct correlation between the potential energy of the droplet and its horizontal acceleration. However, it is noteworthy to see that the initial horizontal velocity for an impact speed of 384 mm/s exhibits a delay in increasing but eventually recovers and accelerates. This behavior occurs when the droplet's centroid aligns exactly with the gap between two bSi strips, and the impact speed is sufficiently high. Under these conditions, the droplet can penetrate the gap, leading to droplet pinning, which consequently impedes the droplet's horizontal acceleration. This phenomenon is visually captured in Figure S8. The findings

in this section will be the critical basis necessary in designing a superhydrophobic ratchet surface to manipulate a droplet employing the Laplace pressure gradient.

**Determination of Critical Conditions for Penetration** through FEA. In the previous section, we discussed the scenario in which a droplet can penetrate the gap between two bSi strips under specific conditions. To prevent this and optimize the operation of our superhydrophobic ratchet surface, we developed an FEA model using COMSOL Multiphysics. In this analysis, we calculated the volume fraction of the droplet that penetrates beneath the gap between the bSi strips while varying several parameters: the gap distance between the bSi strips, the droplet's impact speed, its size and relative viscosity (with the viscosity of deionized water as a reference point set at 1), and the thickness of the bSi strips. The results of this analysis are depicted in Figure 7, in a three-dimensional mesh plot where the x- and y-axes represent the parameters being varied and the z-axis indicates the volume fraction of the droplet that penetrates beneath the gap between the bSi strips. The default values for each parameter are provided in Table S1 in the Supporting Information.

In our prior experiments, a droplet impacting at a speed of 384 mm/s at the gap between the bSi strips experienced penetration. The FEA results for this condition showed that approximately 1% of the droplet's volume penetrating the gap. Accordingly, we

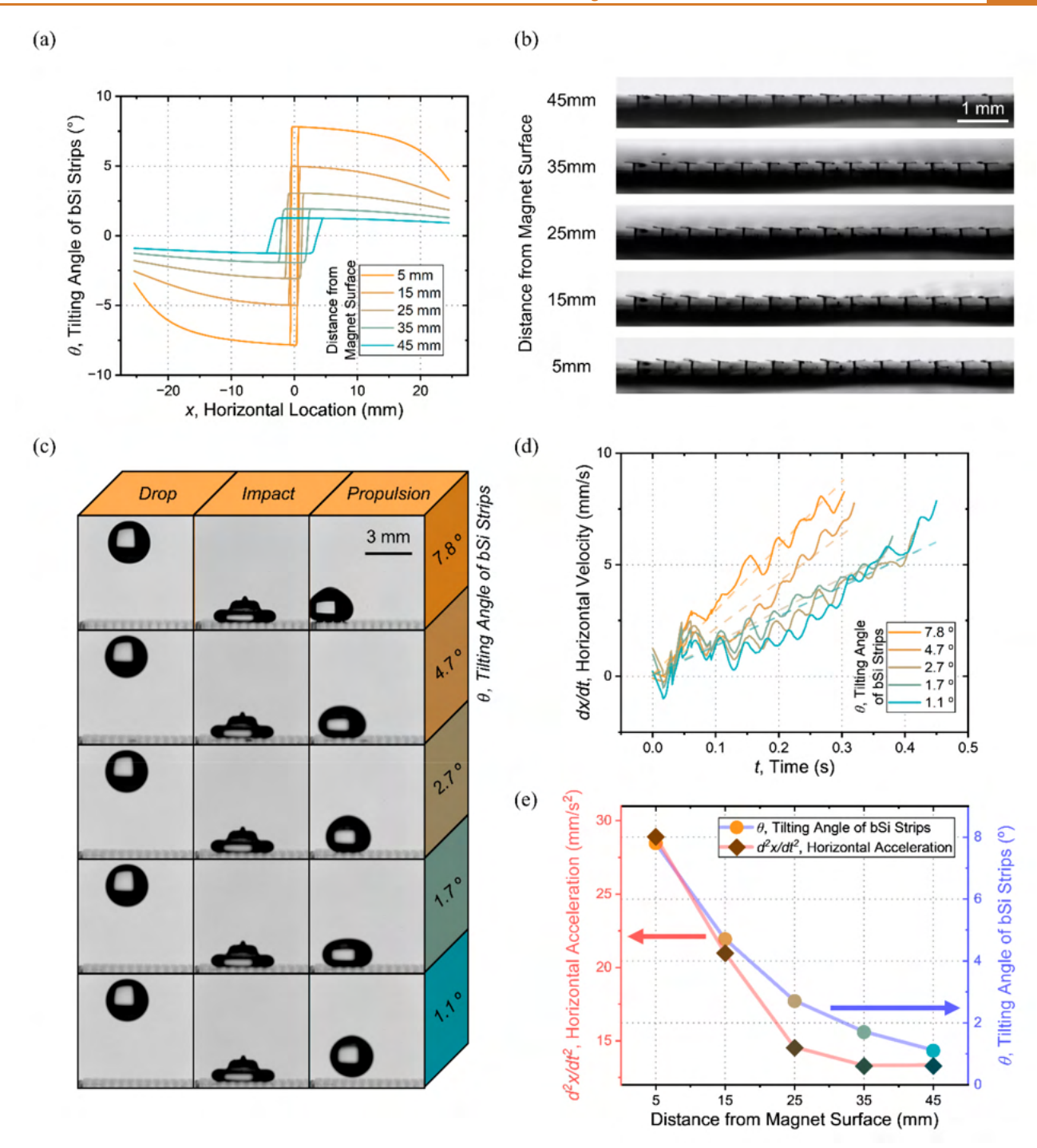
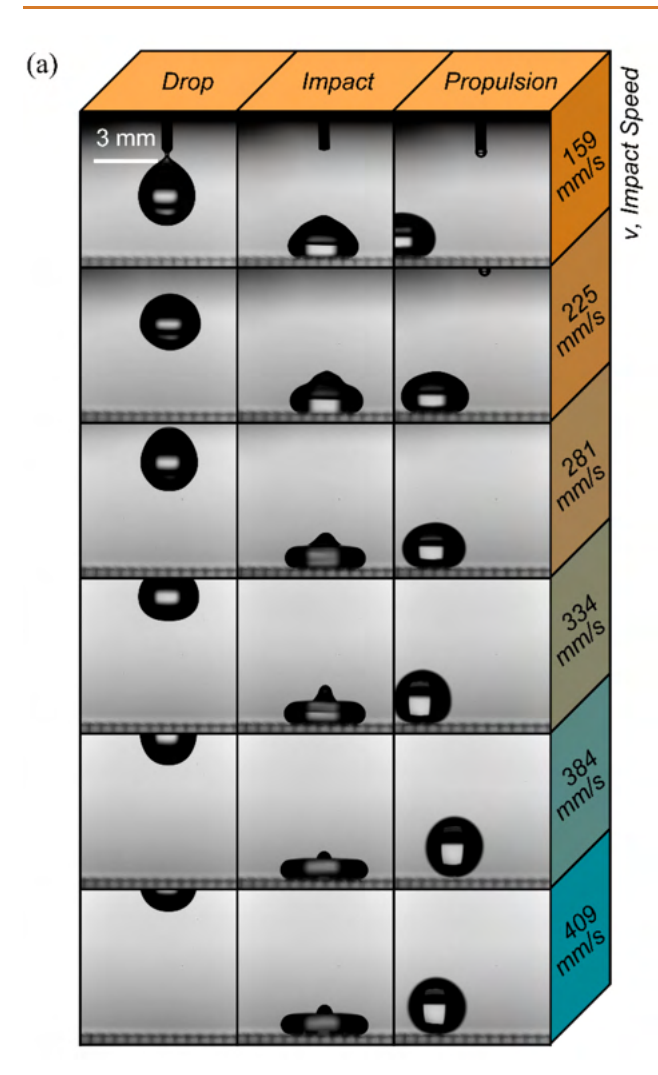


Figure 5. Experimental and theoretical analysis of tilting angles, droplet propulsion, and acceleration. (a) Theoretical tilting angle as a function of the bSi strip's location for various distances from the external magnet surface. (b) Tilted bSi strips with various tilting angles at various distances from the external magnet surface. (c) Frames captured from a high-speed camera movie illustrating the sequential events of droplet fall, impact on the strip, and propulsion. Each row showcases the results corresponding to different tilting angles of bSi strips. (d) Horizontal velocity of the droplet derived from position data obtained through image analysis. The dashed line represents the linear regression for each tilting angle of the bSi strip. (e) The horizontal acceleration plotted against the distance between the bSi strip and the external magnet which also demonstrates a positive correlation between acceleration and the tilting angle of the bSi strip.

define this point as the critical condition, and we have drawn a red solid line across the mesh to indicate the 1% volume fraction. The objective of this analysis is to prevent penetration; therefore, the volume fraction should remain below this red line.

Figure 7a demonstrates that as the gap between the bSi strips increases, the rate of penetration also increases. However, it is evident that the impact speed of the droplet has a more

significant influence on the penetration rate. Figure 7b reveals that not only does a decrease in droplet size increase the probability of penetration but smaller droplets also become more susceptible to penetration as the gap size increases. Figure 7c demonstrates that the viscosity of the droplet has a minimal impact on the penetration rate. Similarly, Figure 7d shows that the thickness of the bSi strips also has little effect on droplet



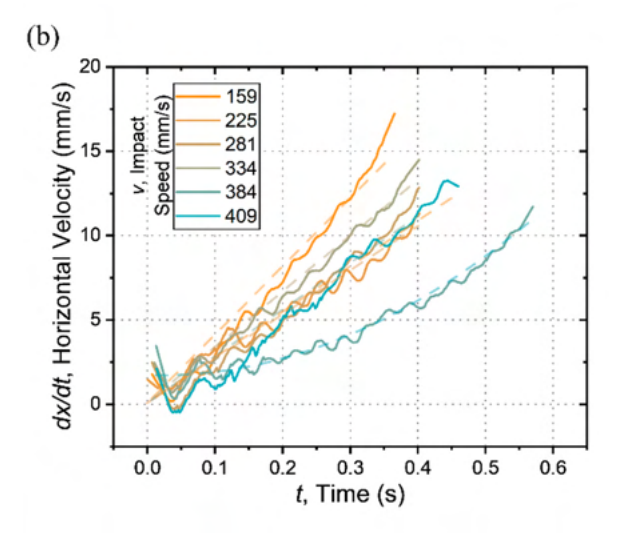


Figure 6. Droplet propulsion analysis upon different impact speeds. (a) Frames captured from a high-speed camera movie illustrating the sequential events of droplet fall, impact on the strip, and propulsion. Each row showcases the results corresponding to different impact speeds of the droplet. (b) Horizontal velocity of the droplet derived from position data obtained through image analysis. The dashed line represents the polynomial fitting for each impact speeds.

penetration. The Weber Number (We) for Figure 7a–c was calculated using the following equation, which incorporates the droplet's viscosity  $(\rho)$ , diameter (D), and surface tension  $(\sigma)$ .

$$We = \frac{\rho v^2 D}{\sigma} \tag{9}$$

#### **CONCLUSION**

In summary, our study demonstrates the successful implementation of bidirectional droplet manipulation on a magnetically actuated superhydrophobic ratchet surface. The soft magnetic properties of the silicon strips allow for bidirectional tilting, enabling efficient droplet manipulation in response to changes in the external magnetic field. Computational multiphysics models have been developed to predict the tilting behavior, providing valuable insights into the concept of bidirectional tilting and the tilting angle hysteresis theory. Experimental results have confirmed the soft magnetic hysteresis, bidirectional tilting of the strips, and consequential bidirectional self-propulsion of dispensed droplets through the Laplace pressure gradient. Additionally, finite element analysis has identified critical conditions for preventing droplet penetration through the gaps between the strips, which is crucial for optimizing droplet manipulation. These findings suggest the way for the design and optimization of magnetically actuated superhydrophobic ratchet surfaces in digital microfluidic applications, promising advances in various fields that rely on precise and instantaneous droplet control.

# **METHODS**

**Fabrication of bSi Strips with NdFeB Layer.** The fabrication of the ratchet surfaces leverages previously developed methods. One such method includes the ability to manipulate, flip, and transfer ultrathin silicon (UTS)—a technique that proves crucial when handling the 15  $\mu$ m silicon film used in this research. <sup>58,65</sup> Another method is the transfer printing technique, which enables the three-dimensional heterogeneous integration of bSi strips and elastomer ridges. <sup>66</sup>

First, as shown in Figure S9, we source UTS from the device layer of a silicon-on-insulator (SOI) wafer (Ultrasil LLC). We pattern the device layer of the SOI wafer with a photoresist (SPR-220, Megaposit) and subsequently deep reactive ion etch (SLR 770, Plasmatherm) it into the desired strip shapes. Following this, we perform a thorough cleaning process, which involves degreasing, a 10 min session of RCA-1 cleaning, and 1 min of 100 W oxygen descumming to effectively remove any organic photoresist residue.

We then form the bSi surface on the device layer, a process that involves three steps in a reactive ion etcher (Oxford). These steps are oxide layer formation in oxygen plasma (50 mT, 10 sccm, RF1/2 120/200 W, 5 min), random scattering of oxide etch (50 mT, CHF3 12 sccm, RF1 350 W, 2 min), and silicon etch with an oxide hard mask (90 mT, Cl2/Ar 40/4 sccm, RF1/2 300/500 W, 10 min).

Following this, we immersed the SOI wafer in a hydrofluoric (HF) acid bath to entirely remove the buried oxide layer. The device layer, which is now the UTS, can self-delaminate under an IPA bath. This free-floating UTS can be picked up and transferred to a mediator substrate with the bSi side facing down. To get a higher yield during the subsequent NdFeB deposition step, we used water-soluble tape to secure the corner of the UTS.

The UTS is placed into a sputtering system (Kurt J. Lesker Company), where layers of Ti/NdFeB/Ti, each measuring 5/335/5 nm, respectively, are deposited on its backside. The NdFeB deposition takes place over 50 min, achieving a slow deposition rate of 6.7 nm/min. This slow rate results in a smaller grain size, which in turn results in the material exhibiting soft magnetic behavior. The UTS is then covered with photoresist and a silane-coated glass slide to ensure it remains firmly fixed while it undergoes initial magnetization in the width

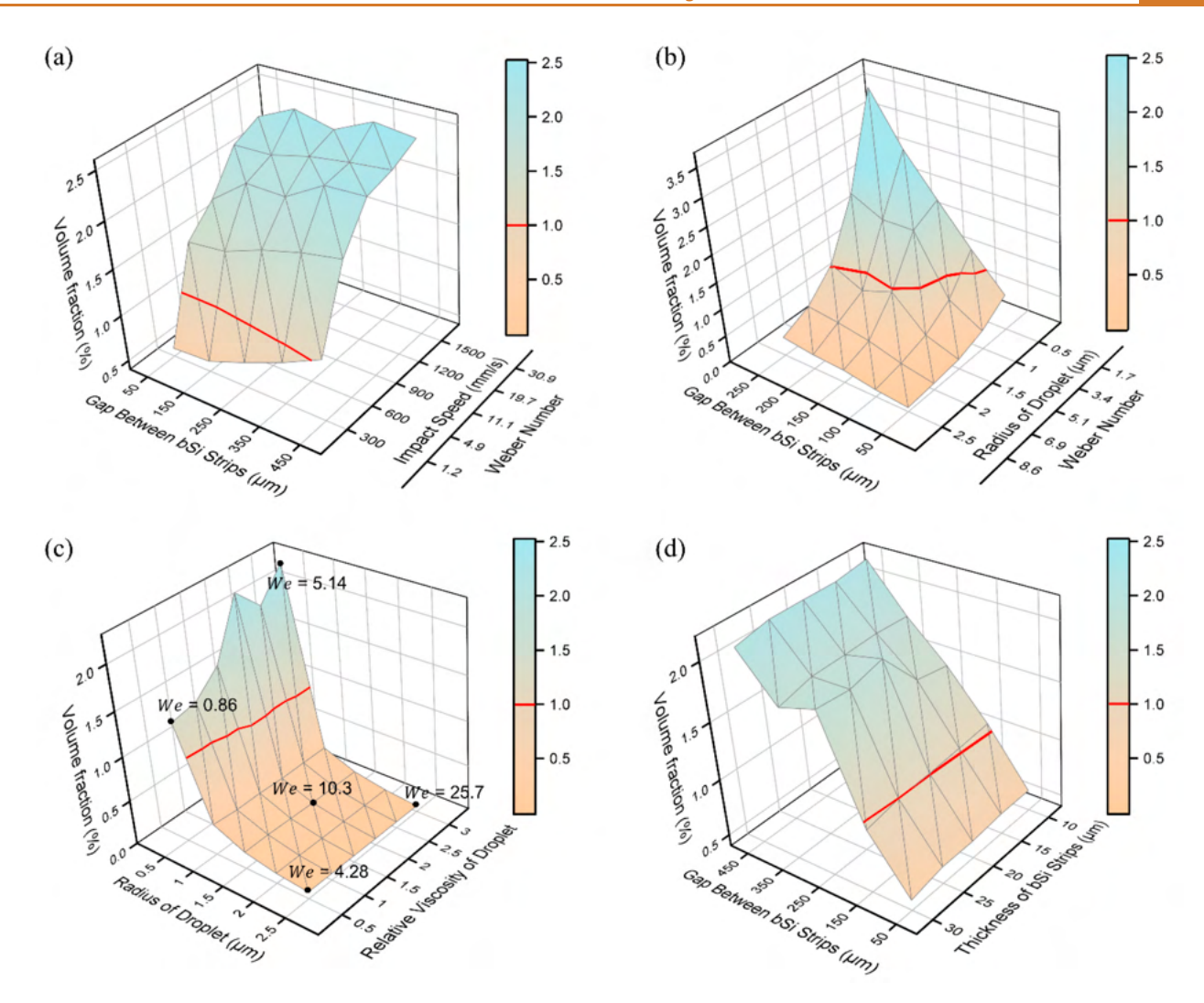


Figure 7. FEA analysis identifies critical conditions for droplet penetration. The volume fraction representing the proportion of the droplet that penetrates through the bSi strips under each parameter set, as determined through FEA. Different sets of parameters were chosen as inputs for (a) the gap between the bSi strips and the impact speed of a droplet, (b) the gap between the bSi strips and the radius of the droplet, (c) the radius of the droplet and the relative viscosity of the droplet, and (d) the gap between the bSi strips and the thickness of the bSi skins. The red solid line indicates the 1.0% penetration of the droplet, which is regarded as a critical condition.

direction (5 T impulse field, Magnet-Physics Inc.). After magnetization, the UTS is degreased to prepare for transfer printing.

Fabrication of Elastomer Ridges. The fabrication of the elastomer ridges that hold the bSi strips is achieved using a molding method, as depicted in Figure S10. To create the mold, we spin coat a silicon wafer (UniversityWafer, Inc.) with SU8 (SU-8 100, Kayaku Advanced Materials) at 2500 rpm for 60 s. This is followed by a short soft bake for 1 min at 65 °C and 4 min at 95 °C. We repeat the spincoating process twice more, giving us three total layers of SU8, with same short soft bakes taking place between the second and third layers. After the third layer, the final soft bake lasts for 30 min at 65 °C and 90 min at 95 °C. The Si-SU8 mold then undergoes flood exposure under a flood exposure system (ABM Model 60), covered with an iron oxide mask until it receives a dose of 500 mJ/cm<sup>2</sup>. The mold is then postexposure baked for 1 min at 65 °C and 35 min at 95 °C. Next, we immerse the mold in SU-8 developer (Kayaku Advanced Materials) for 30 min or until fully developed. To finish, we coat the mold with a single layer of FDTS using a Molecular Vapor Deposition (MVD Model 100, Applied MicroStructures) and pour Polydimethylsiloxane (PDMS) with a base to curing agent ratio of 10:1 over the mold and then allow it to cure. Once cured, the elastomer (PDMS) ridges are demolded.

Transfer Printing bSi Strips onto Elastomer Ridges. In the final stages, the transfer printing technique is utilized for the heterogeneous

integration of the UTS and elastomer ridges as illustrated in Figure S11. At first, an uncured PDMS solution (with a 10:1 base to curing agent ratio) is spin-coated onto a glass slide at 5000 rpm for 30 s. The tips of the elastomer ridges are then dipped into this thin layer of PDMS and transferred to a clean glass slide, with the ridge side facing downward. This assembly is partially cured at 65 °C for 15 min. Afterward, the elastomer ridge is affixed to the mask fixture of a mask aligner (MJB3, Karl Suss), with the UTS positioned on the sample holder chuck. The elastomer ridges are then meticulously aligned to lift the UTS. After the UTS has been transferred on the elastomer ridges, the tethers securing the bSi strips to the UTS can be physically broken, allowing for the individual separation of all the strips. A final coating of FDTS is applied to the bSi side, facilitating the formation of a superhydrophobic surface.

**High Speed Camera Setup.** The experimental test setup is shown in Figure S12. The motion of the water droplet was captured using a high-speed camera (FASTCAM Mini AX200, Photron) set to a frame rate of 6400 fps and a resolution of  $1024 \times 1024$  pixels. An LED light source, powered by a power supply, was used to illuminate the scene and facilitate the identification of the droplet's identification. For the uniform dispensing of the DI water droplet, a syringe pump (11 Pico Plus Elite, Harvard Apparatus) was employed. The syringe on the pump was connected to a blunt-ended stainless steel needle via a tube, with the needle held in place on an XYZ-axis linear stage. Sequentially, the

ratchet surface and external magnet were positioned below the needle. The arrangement of the needle, ratchet surface, and external magnet depended on the experiment being conducted. When exploring the relationship between the tilting angle of the bSi strips and the propulsion force, we affixed the needle and the ratchet surface as one entity to the Z-axis linear stage. Meanwhile, the external magnet was placed on the XY-axis linear stage. On the other hand, during the test aimed at understanding the relationship between the potential energy of the droplet and the propulsion force, we relocated the ratchet surface to the external magnet's top surface.

Multiphysics FEA Modeling and Its Constraints and **Conditions.** Given the computational limitations, we chose a twodimensional axisymmetric design for our analysis. The model's geometry includes the droplet, the bSi structure, and two air regions located above and below the bSi strips. We set the top wall as a "no slip" condition, while the side wall was assigned an outlet condition. The walls for both the bSi and the PDMS were defined as wetted walls, with a contact angle of 170 degrees. To allow the droplet to fall, gravity was implemented within the system. The analysis incorporated two physics entities, the Laminar Flow and Level Set, combined into a single Multiphysics simulation. The study was performed in a time-dependent solver with two independent parametric sweeps. The volume fraction, which represents the volume of water below the level of the bSi strips divided by the volume of the original droplet, is computed at each time step. We have provided an example of a single run for this model in Movie S6.

#### ASSOCIATED CONTENT

# Supporting Information

The Supporting Information is available free of charge at https://pubs.acs.org/doi/10.1021/acsnano.3c07360.

Figure S1: bSi strip coated with gold on one side exhibiting soft magnetic behavior; Figure S2: Computational multiphysics modeling results with a cylindrical permanent magnet; Figure S3: The BH curves illustrating the magnetic hysteresis behavior; Figure S4: Magnetic field strength or flux density for other components; Figure S5: The curvature of the leading and trailing sides of the droplet and the direction of the Laplace pressure gradient; Figure S6: (a) The frames of movie being image processed to identify the position of the droplet; (b) the resulting horizontal position of the droplet plotted over time; Figure S7: The (a) horizontal and (b) vertical position of the droplet plotted over time; (c) the vertical position differentiated into the vertical velocity; (d) the average horizontal acceleration for each impact speed; Figure S8: The penetration observed at the impact speed of 334 mm/s; Figure S9: Fabrication of bSi strips with a magnetic layer; Figure S10: Fabrication of PDMS elastomer ridges; Figure S11: Transfer printing of bSi strips onto elastomer ridges; Figure S12: The experimental test setup for droplet motion capture; Table S1: Default values for each parameter in FEA (PDF)

Movie S1: Bidirectional droplet manipulation captured by a camera (MP4)

Movie S2: High-speed camera recording of bidirectional droplet manipulation; the top row shows the camera focused on the droplet, while the bottom row focuses on the strips (MP4)

Movie S3: Switching of bSi strip's magnetization direction (MP4)

Movie S4: Impact of tilting angle of bSi strips on propulsion force (MP4)

Movie S5: Effect of impact speeds on propulsion force (MP4)

Movie S6: Demonstration of the FEA model (MP4)

## **AUTHOR INFORMATION**

#### Corresponding Author

Seok Kim — Department of Mechanical Engineering, Pohang University of Science and Technology, Pohang 37673, South Korea; Department of Mechanical Science and Engineering, University of Illinois at Urbana—Champaign, Urbana, Illinois 61801, United States; Institute for Convergence Research and Education in Advanced Technology, Yonsei University, Seoul 03722, South Korea; ◎ orcid.org/0000-0003-3206-8061; Email: seok.kim@postech.ac.kr

#### **Authors**

ChangHee Son — Department of Mechanical Science and Engineering, University of Illinois at Urbana—Champaign, Urbana, Illinois 61801, United States; orcid.org/0000-0002-2985-5251

Zhengyu Yang — Department of Mechanical Science and Engineering, University of Illinois at Urbana—Champaign, Urbana, Illinois 61801, United States

Seungbeom Kim — Department of Mechanical Engineering, Pohang University of Science and Technology, Pohang 37673, South Korea

Placid M. Ferreira — Department of Mechanical Science and Engineering, University of Illinois at Urbana—Champaign, Urbana, Illinois 61801, United States

Jie Feng — Department of Mechanical Science and Engineering, University of Illinois at Urbana—Champaign, Urbana, Illinois 61801, United States; Materials Research Laboratory, University of Illinois at Urbana—Champaign, Urbana, Illinois 61801, United States; orcid.org/0000-0002-4891-9214

Complete contact information is available at: https://pubs.acs.org/10.1021/acsnano.3c07360

## **Author Contributions**

C.S. and Seok K. conceived the idea. C.S., Z.Y., and Seungbeom K. performed the experimental studies. C.S., Z.Y., and Seungbeom K. carried out the analysis. C.S. and Seungbeom K. contributed to the sample fabrications. C.S. created the computational model. C.S. designed the FEA model. Seok K. acquired funding. C.S. wrote the manuscript. All authors read and revised the manuscript. P.M.F., J.F., and Seok K. supervised the work.

# Notes

The authors declare no competing financial interest.

# **ACKNOWLEDGMENTS**

This work was supported by the National Science Foundation (ECCS-1950009) and the National Research Foundation of Korea (NRF) funded by Ministry of Science and ICT (2022M317A3050820; 2022R1A4A3033320; 2022R1A2C3006420).

# **ABBREVIATIONS**

NdFeB, neodymium—iron—boron; bSi, black silicon; FDTS, perfluorodecyltrichlorosilane; FEA, finite element analysis; UTS, ultrathin silicon; SOI, silicon-on-insulator; HF, hydrofluoric; PDMS, polydimethylsiloxane.

#### **REFERENCES**

- (1) Sun, D.; Böhringer, K. F. An Active Self-Cleaning Surface System for Photovoltaic Modules Using Anisotropic Ratchet Conveyors and Mechanical Vibration. *Microsyst. Nanoeng.* **2020**, *6* (1), 1–12.
- (2) Tan, C. L. C.; Sapiha, K.; Leong, Y. F. H.; Choi, S.; Anariba, F.; Thio, B. J. R. Lotus-like Effect for Metal Filings Recovery and Particle Removal on Heated Metal Surfaces Using Leidenfrost Water Droplets. *Soft Matter* **2015**, *11* (27), 5400–5407.
- (3) Zheng, Y.; Bai, H.; Huang, Z.; Tian, X.; Nie, F.-Q.; Zhao, Y.; Zhai, J.; Jiang, L. Directional Water Collection on Wetted Spider Silk. *Nature* **2010**, 463 (7281), 640–643.
- (4) Nightingale, A. M.; Phillips, T. W.; Bannock, J. H.; de Mello, J. C. Controlled Multistep Synthesis in a Three-Phase Droplet Reactor. *Nat. Commun.* **2014**, *5* (1), 3777.
- (5) Bawazer, L. A.; McNally, C. S.; Empson, C. J.; Marchant, W. J.; Comyn, T. P.; Niu, X.; Cho, S.; McPherson, M. J.; Binks, B. P.; deMello, A.; Meldrum, F. C. Combinatorial Microfluidic Droplet Engineering for Biomimetic Material Synthesis. *Sci. Adv.* **2016**, 2 (10), No. e1600567.
- (6) Shin, S.; Seo, J.; Han, H.; Kang, S.; Kim, H.; Lee, T. Bio-Inspired Extreme Wetting Surfaces for Biomedical Applications. *Materials* **2016**, 9 (2), 116.
- (7) Ai, Y.; Xie, R.; Xiong, J.; Liang, Q. Microfluidics for Biosynthesizing: From Droplets and Vesicles to Artificial Cells. *Small* **2020**, *16* (9), 1903940.
- (8) Zhang, Y.; Wang, T.-H. Full-Range Magnetic Manipulation of Droplets via Surface Energy Traps Enables Complex Bioassays. *Adv. Mater.* **2013**, 25 (21), 2903–2908.
- (9) Su, F.; Ozev, S.; Chakrabarty, K. Ensuring the Operational Health of Droplet-Based Microelectrofluidic Biosensor Systems. *IEEE Sens. J.* **2005**, *5* (4), 763–773.
- (10) Regan, D. P.; Howell, C. Droplet Manipulation with Bioinspired Liquid-Infused Surfaces: A Review of Recent Progress and Potential for Integrated Detection. *Curr. Opin. Colloid Interface Sci.* **2019**, 39, 137–147.
- (11) Yang, C.; Zeng, Q.; Huang, J.; Guo, Z. Droplet Manipulation on Superhydrophobic Surfaces Based on External Stimulation: A Review. *Adv. Colloid Interface Sci.* **2022**, *306*, 102724.
- (12) Zhu, G.-P.; Wang, Q.-Y.; Ma, Z.-K.; Wu, S.-H.; Guo, Y.-P. Droplet Manipulation under a Magnetic Field: A Review. *Biosensors* **2022**, *12* (3), 156.
- (13) Zhang, Y.; Nguyen, N.-T. Magnetic Digital Microfluidics a Review. Lab. Chip 2017, 17 (6), 994–1008.
- (14) Long, Z.; Shetty, A. M.; Solomon, M. J.; Larson, R. G. Fundamentals of Magnet-Actuated Droplet Manipulation on an Open Hydrophobic Surface. *Lab. Chip* **2009**, *9* (11), 1567–1575.
- (15) Shin, D. J.; Wang, T.-H. Magnetic Droplet Manipulation Platforms for Nucleic Acid Detection at the Point of Care. *Ann. Biomed. Eng.* **2014**, 42 (11), 2289–2302.
- (16) Lee, K. Y.; Park, S.; Lee, Y. R.; Chung, S. K. Magnetic Droplet Microfluidic System Incorporated with Acoustic Excitation for Mixing Enhancement. *Sens. Actuators Phys.* **2016**, 243, 59–65.
- (17) Huang, G.; Li, M.; Yang, Q.; Li, Y.; Liu, H.; Yang, H.; Xu, F. Magnetically Actuated Droplet Manipulation and Its Potential Biomedical Applications. ACS Appl. Mater. Interfaces 2017, 9 (2), 1155–1166.
- (18) Tsuchiya, H.; Okochi, M.; Nagao, N.; Shikida, M.; Honda, H. On-Chip Polymerase Chain Reaction Microdevice Employing a Magnetic Droplet-Manipulation System. *Sens. Actuators B Chem.* **2008**, *130* (2), 583–588.
- (19) Li, A.; Li, H.; Li, Z.; Zhao, Z.; Li, K.; Li, M.; Song, Y. Programmable Droplet Manipulation by a Magnetic-Actuated Robot. *Sci. Adv.* **2020**, *6* (7), No. eaay5808.
- (20) Zhang, Y.; Jiang, S.; Hu, Y.; Wu, T.; Zhang, Y.; Li, H.; Li, A.; Zhang, Y.; Wu, H.; Ding, Y.; Li, E.; Li, J.; Wu, D.; Song, Y.; Chu, J. Reconfigurable Magnetic Liquid Metal Robot for High-Performance Droplet Manipulation. *Nano Lett.* **2022**, 22 (7), 2923–2933.
- (21) Chiou, C.-H.; Jin Shin, D.; Zhang, Y.; Wang, T.-H. Topography-Assisted Electromagnetic Platform for Blood-to-PCR in a Droplet. *Biosens. Bioelectron.* **2013**, *50*, 91–99.

- (22) Yang, C.; Li, G. A Novel Magnet-Actuated Droplet Manipulation Platform Using a Floating Ferrofluid Film. Sci. Rep. 2017, 7 (1), 15705.
- (23) Bijarchi, M. A.; Favakeh, A.; Sedighi, E.; Shafii, M. B. Ferrofluid Droplet Manipulation Using an Adjustable Alternating Magnetic Field. Sens. Actuators Phys. **2020**, 301, 111753.
- (24) Zhang, K.; Liang, Q.; Ma, S.; Mu, X.; Hu, P.; Wang, Y.; Luo, G. On-Chip Manipulation of Continuous Picoliter-Volume Superparamagnetic Droplets Using a Magnetic Force. *Lab. Chip* **2009**, *9* (20), 2992–2999.
- (25) Irajizad, P.; Ray, S.; Farokhnia, N.; Hasnain, M.; Baldelli, S.; Ghasemi, H. Remote Droplet Manipulation on Self-Healing Thermally Activated Magnetic Slippery Surfaces. *Adv. Mater. Interfaces* **2017**, *4* (12), 1700009.
- (26) Nasirimarekani, V.; Benito-Lopez, F.; Basabe-Desmonts, L. Tunable Superparamagnetic Ring (tSPRing) for Droplet Manipulation. *Adv. Funct. Mater.* **2021**, 31 (32), 2100178.
- (27) Aussillous, P.; Quéré, D. Liquid Marbles. *Nature* **2001**, 411 (6840), 924–927.
- (28) McHale, G.; Newton, M. I. Liquid Marbles: Principles and Applications. *Soft Matter* **2011**, *7* (12), 5473–5481.
- (29) Zhao, Y.; Xu, Z.; Parhizkar, M.; Fang, J.; Wang, X.; Lin, T. Magnetic Liquid Marbles, Their Manipulation and Application in Optical Probing. *Microfluid. Nanofluidics* **2012**, *13* (4), 555–564.
- (30) Zhao, Y.; Fang, J.; Wang, H.; Wang, X.; Lin, T. Magnetic Liquid Marbles: Manipulation of Liquid Droplets Using Highly Hydrophobic Fe3O4 Nanoparticles. *Adv. Mater.* **2010**, 22 (6), 707–710.
- (31) Zhao, Y.; Xu, Z.; Niu, H.; Wang, X.; Lin, T. Magnetic Liquid Marbles: Toward "Lab in a Droplet. Adv. Funct. Mater. 2015, 25 (3), 437–444
- (32) Guo, J.; Wang, D.; Sun, Q.; Li, L.; Zhao, H.; Wang, D.; Cui, J.; Chen, L.; Deng, X. Omni-Liquid Droplet Manipulation Platform. *Adv. Mater. Interfaces* **2019**, *6* (16), 1900653.
- (33) Yang, C.; Zhang, Z.; Li, G. Programmable Droplet Manipulation by Combining a Superhydrophobic Magnetic Film and an Electromagnetic Pillar Array. Sens. Actuators B Chem. 2018, 262, 892–901.
- (34) Fang, Y.; Liang, J.; Bai, X.; Yong, J.; Huo, J.; Yang, Q.; Hou, X.; Chen, F. Magnetically Controllable Isotropic/Anisotropic Slippery Surface for Flexible Droplet Manipulation. *Langmuir* **2020**, *36* (50), 15403–15409.
- (35) Chu, L.; Li, W.; Zhan, Y.; Amirfazli, A. Magnetically Responsive Superhydrophobic Surfaces with Droplet Manipulation Capability. *Adv. Eng. Mater.* **2023**, 25 (8), 2201352.
- (36) Guo, P.; Wang, Z.; Heng, L.; Zhang, Y.; Wang, X.; Jiang, L. Magnetocontrollable Droplet and Bubble Manipulation on a Stable Amphibious Slippery Gel Surface. *Adv. Funct. Mater.* **2019**, 29 (11), 1808717.
- (37) Zhan, Y.; Yu, S.; Amirfazli, A.; Siddiqui, A. R.; Li, W. Magnetically Responsive Superhydrophobic Surfaces for Microdroplet Manipulation. *Adv. Mater. Interfaces* **2022**, *9* (5), 2102010.
- (38) Jiang, S.; Hu, Y.; Wu, H.; Zhang, Y.; Zhang, Y.; Wang, Y.; Zhang, Y.; Zhu, W.; Li, J.; Wu, D.; Chu, J. Multifunctional Janus Microplates Arrays Actuated by Magnetic Fields for Water/Light Switches and Bio-Inspired Assimilatory Coloration. *Adv. Mater.* **2019**, *31* (15), 1807507.
- (39) Jing, X.; Chen, H.; Zhang, L.; Zhao, S.; Wang, Y.; Wang, Z.; Zhou, Y. Accurate Magneto-Driven Multi-Dimensional Droplet Manipulation. *Adv. Funct. Mater.* **2023**, 33 (9), 2210883.
- (40) Yang, C.; Wu, L.; Li, G. Magnetically Responsive Superhydrophobic Surface: In Situ Reversible Switching of Water Droplet Wettability and Adhesion for Droplet Manipulation. *ACS Appl. Mater. Interfaces* **2018**, *10* (23), 20150–20158.
- (41) Ben, S.; Zhou, T.; Ma, H.; Yao, J.; Ning, Y.; Tian, D.; Liu, K.; Jiang, L. Multifunctional Magnetocontrollable Superwettable-Microcilia Surface for Directional Droplet Manipulation. *Adv. Sci.* **2019**, *6* (17), 1900834.
- (42) Demirörs, A. F.; Aykut, S.; Ganzeboom, S.; Meier, Y. A.; Poloni, E. Programmable Droplet Manipulation and Wetting with Soft Magnetic Carpets. *Proc. Natl. Acad. Sci. U. S. A.* **2021**, *118* (46), No. e2111291118.

- (43) Kim, J. H.; Kang, S. M.; Lee, B. J.; Ko, H.; Bae, W.-G.; Suh, K. Y.; Kwak, M. K.; Jeong, H. E. Remote Manipulation of Droplets on a Flexible Magnetically Responsive Film. *Sci. Rep.* **2015**, *5* (1), 17843.
- (44) Wang, W.; Lai, H.; Cheng, Z.; Fan, Z.; Zhang, D.; Wang, J.; Yu, S.; Xie, Z.; Liu, Y. Superhydrophobic Shape Memory Polymer Microarrays with Switchable Directional/Antidirectional Droplet Sliding and Optical Performance. ACS Appl. Mater. Interfaces 2020, 12 (43), 49219–49226.
- (45) Lin, Y.; Hu, Z.; Zhang, M.; Xu, T.; Feng, S.; Jiang, L.; Zheng, Y. Magnetically Induced Low Adhesive Direction of Nano/Micropillar Arrays for Microdroplet Transport. *Adv. Funct. Mater.* **2018**, 28 (49), 1800163.
- (46) Qian, C.; Zhou, F.; Wang, T.; Li, Q.; Hu, D.; Chen, X.; Wang, Z. Pancake Jumping of Sessile Droplets. *Adv. Sci.* **2022**, *9* (7), 2103834.
- (47) Li, C.; Jiao, Y.; Zhang, Y.; Jiang, S.; Lv, X.; Wu, S.; Li, J.; Hu, Y.; Ye, J.; Liu, K.; Wu, D.; Chu, J. Noncontact All-In-Situ Reversible Reconfiguration of Femtosecond Laser-Induced Shape Memory Magnetic Microcones for Multifunctional Liquid Droplet Manipulation and Information Encryption. *Adv. Funct. Mater.* **2021**, 31 (20), 2100543.
- (48) Wang, J.; Zhu, Z.; Liu, P.; Yi, S.; Peng, L.; Yang, Z.; Tian, X.; Jiang, L. Magneto-Responsive Shutter for On-Demand Droplet Manipulation. *Adv. Sci.* **2021**, *8* (23), 2103182.
- (49) Yang, C.; Ning, Y.; Ku, X.; Zhuang, G.; Li, G. Automatic Magnetic Manipulation of Droplets on an Open Surface Using a Superhydrophobic Electromagnet Needle. *Sens. Actuators B Chem.* **2018**, 257, 409–418.
- (50) Zhou, A.; Xu, C.; Kanitthamniyom, P.; Ng, C. S. X.; Lim, G. J.; Lew, W. S.; Vasoo, S.; Zhang, X.; Lum, G. Z.; Zhang, Y. Magnetic Soft Millirobots 3D Printed by Circulating Vat Photopolymerization to Manipulate Droplets Containing Hazardous Agents for In Vitro Diagnostics. *Adv. Mater.* **2022**, 34 (15), 2200061.
- (51) Yang, Z.; Park, J. K.; Kim, S. Magnetically Responsive Elastomer—Silicon Hybrid Surfaces for Fluid and Light Manipulation. *Small* **2018**, *14* (2), 1702839.
- (52) Son, C.; Ji, B.; Park, J.; Feng, J.; Kim, S. A Magnetically Actuated Superhydrophobic Ratchet Surface for Droplet Manipulation. *Micromachines* **2021**, *12* (3), 325.
- (53) Feng, S.; Zhu, P.; Zheng, H.; Zhan, H.; Chen, C.; Li, J.; Wang, L.; Yao, X.; Liu, Y.; Wang, Z. Three-Dimensional Capillary Ratchet-Induced Liquid Directional Steering. *Science* **2021**, 373 (6561), 1344–1348.
- (54) Herzer, G. Grain Size Dependence of Coercivity and Permeability in Nanocrystalline Ferromagnets. *IEEE Trans. Magn.* **1990**, 26 (5), 1397–1402.
- (55) Bao, L.; Yun, G.; Bai, N.; Cao, Y. Grain-Size Effect on Coercivity of Nd–Fe–B Nanomagnets: Micromagnetics Simulation Based on a Multi-Grain Model. *Appl. Phys. Express* **2021**, *14* (8), 085505.
- (56) Rahimi, H.; Ghasemi, A.; Mozaffarinia, R. Coercivity Mechanism in Nd-Fe-B Nanoparticles Synthesized by Reduction-Diffusion Process. *J. Supercond. Nov. Magn.* **2016**, 29 (8), 2099–2107.
- (57) Camacho, J. M.; Sosa, V. Alternative Method to Calculate the Magnetic Field of Permanent Magnets with Azimuthal Symmetry. *Rev. Mex. Fisica E* **2013**, 59 (1), 8–17.
- (58) Son, C.; Lee, S.; Ferreira, P. M.; Kim, S. Dual Coil Patterned Ultra-Thin Silicon Film Enable by Double-Sided Process. *Adv. Mater. Interfaces* **2023**, *10* (16), 2300158.
- (59) Blinder, S. M. Magnetic Field of a Cylindrical Bar Magnet. Wolfram Demonstrations Project. http://demonstrations.wolfram.com/MagneticFieldOfACylindricalBarMagnet/ (accessed on July 5, 2023).
- (60) Gillies, A. G.; Kwak, J.; Fearing, R. S. Controllable Particle Adhesion with a Magnetically Actuated Synthetic Gecko Adhesive. *Adv. Funct. Mater.* **2013**, 23 (26), 3256–3261.
- (61) Bai, H.; Tian, X.; Zheng, Y.; Ju, J.; Zhao, Y.; Jiang, L. Direction Controlled Driving of Tiny Water Drops on Bioinspired Artificial Spider Silks. *Adv. Mater.* **2010**, 22 (48), 5521–5525.
- (62) Wang, Q.; Yang, F.; Guo, Z. Design and Construction of a Laplace and Wettability Gradient Field for Efficient Water Collection. *Chem. Commun.* **2023**, *59* (40), 6048–6051.

- (63) Yan, X.; Qin, Y.; Chen, F.; Zhao, G.; Sett, S.; Hoque, M. J.; Rabbi, K. F.; Zhang, X.; Wang, Z.; Li, L.; Chen, F.; Feng, J.; Miljkovic, N. Laplace Pressure Driven Single-Droplet Jumping on Structured Surfaces. ACS Nano 2020, 14 (10), 12796–12809.
- (64) Yang, J.-T.; Chen, J. C.; Huang, K.-J.; Yeh, J. A. Droplet Manipulation on a Hydrophobic Textured Surface with Roughened Patterns. J. Microelectromechanical Syst. 2006, 15 (3), 697–707.
- (65) Park, J. K.; Zhang, Y.; Xu, B.; Kim, S. Pattern Transfer of Large-Scale Thin Membranes with Controllable Self-Delamination Interface for Integrated Functional Systems. *Nat. Commun.* **2021**, *12* (1), 6882. (66) Kim, S.; Carlson, A.; Cheng, H.; Lee, S.; Park, J.-K.; Huang, Y.; Rogers, J. A. Enhanced Adhesion with Pedestal-Shaped Elastomeric Stamps for Transfer Printing. *Appl. Phys. Lett.* **2012**, *100* (17), 171909.